

Topological rainbow trapping of sound waves in synthesized three-dimensional space for square lattice

Jie-Yu Lu(卢杰煜), Shi-Feng Li(李石峰), Xin Li(李鑫), Xin-Ye Zou(邹欣晔), and Jian-Chun Cheng(程建春)

Citation : Chin. Phys. B, 2025, 34 (**2**): 024302. DOI: 10.1088/1674-1056/ada1c5
Journal homepage: http://cpb.iphy.ac.cn; http://iopscience.iop.org/cpb

What follows is a list of articles you may be interested in

Energy-distributable waterborne acoustic launcher for directional sensing

Tian Yang(杨天), Wenting Gao(高文婷), Shida Fan(范世达), Jie Ren(任捷), and Tianzhi Yang(杨天智)
Chin. Phys. B, 2023, 32 (**12**): 124302. DOI: 10.1088/1674-1056/acf5cf

Broadband topological valley-projected edge-states transport in composite structure phononic crystal

Hong-Yong Mao(毛鸿勇), Fu-Jia Chen(陈福家), Kai Guo(郭凯), and Zhong-Yi Guo(郭忠义)
Chin. Phys. B, 2021, 30 (**8**): 084302. DOI: 10.1088/1674-1056/abea89

Symmetry-controlled edge states in graphene-like topological sonic crystal

Zhang-Zhao Yang(杨彰昭), Jin-Heng Chen(陈晋恒), Yao-Yin Peng(彭尧吟), and Xin-Ye Zou(邹欣晔)†
Chin. Phys. B, 2020, 29 (**10**): 104302. DOI: 10.1088/1674-1056/ab9c0e

Acoustic-electromagnetic slow waves in a periodical defective piezoelectric slab

Xiao-juan Li(李小娟), Huan Ge(葛欢), Li Fan(范理), Shu-yi Zhang(张淑仪), Hui Zhang(张辉), Jin Ding(丁劲)
Chin. Phys. B, 2017, 26 (**7**): 074302. DOI: 10.1088/1674-1056/26/7/074302

Homogenization theory for designing graded viscoelastic sonic crystals

Qu Zhao-Liang (曲兆亮), Ren Chun-Yu (任春雨), Pei Yong-Mao (裴永茂), Fang Dai-Ning (方岱宁)
Chin. Phys. B, 2015, 24 (**2**): 024303. DOI: 10.1088/1674-1056/24/2/024303

Topological rainbow trapping of sound waves in synthesized three-dimensional space for square lattice

Jie-Yu Lu(卢杰煜), Shi-Feng Li(李石峰), Xin Li(李鑫),
Xin-Ye Zou(邹欣晔)†, and Jian-Chun Cheng(程建春)

Key Laboratory of Modern Acoustics, Ministry of Education (MOE), Institute of Acoustics, Department of Physics, Collaborative Innovation Center of Advanced Microstructures, Nanjing University, Nanjing 210093, *China*

(Received 2 October 2024; revised manuscript received 19 December 2024; accepted manuscript online 20 December 2024)

The three-dimensional (3D) synthetic space offers a platform for exploring the valley Hall insulator, which is usually constructed in graphene lattice. Here, based on the valley transports in the square lattice, we construct a synthetic space by treating the rotation angle as the third dimension and observe the emergent Weyl points in this synthetic space. Since the construction of synthetic Weyl points results in the formation of edge states between the phononic crystal (PC) and the hard boundary, and the factors of rotation angle and the distance from the PC to the hard boundary affect the frequency of these edge states, we can construct topological rainbow concentrator based on the above principles. We conduct a comprehensive numerical and experimental study to explore the characteristics of topological rainbow concentrators. This work may play a driving role in the development of topological rainbow devices.

Keywords: topological rainbow concentrator, edge states, square lattice

PACS: 43.35.Gk, 03.65.Vf

DOI: 10.1088/1674-1056/ada1c5 **CSTR:** 32038.14.CPB.ada1c5

1. Introduction

Rainbow trapping is a phenomenon in which waves of different frequencies can be captured at different spatial positions, and it has been implemented in optical,[1–6] acoustic,[7–11] and mechanical wave systems.[12–14] Recently, researchers have combined topological states[15–27] with rainbow trapping, so that the manipulated waves have the advantages of robustness and unidirectionality. The synthetic dimension is one of the methods to achieve rainbow trapping, which alters the dispersion relation of topological edge states. The research on acoustic topological rainbow trapping has driven the development of innovative acoustic materials. These materials are capable of controlling the propagation of sound waves and effectively channeling and focusing acoustic energy, thereby transcending the constraints of conventional materials.

Weyl points denote the special points that arise when the non-degenerate conduction and valence bands of a Weyl semimetal intersect in the vicinity of the Fermi level within the 3D momentum space.[28–35] And Weyl points possess a host of unique properties, including chiral anomalies, topological Fermi arcs and edge states. Recently, scholars have delved into the topological characteristics of Weyl points within an artificial 3D parameter space.[36–43] In this context, the synthetic space is engineered by incorporating one extra structural parametric dimension alongside the conventional physical dimension. Also, synthetic Weyl points possess such a property that they can induce topological edge states at the boundary between the phononic crystal (PC) and rigid boundaries or photonic crystals and any reflection substrates.[38–43] Wang *et al.* have utilized this property to probe two different types of topological rainbow concentrators related to the acoustic valley Hall insulator.[8] However, the research on synthetic Weyl points has mostly been conducted in two-dimensional (2D) graphene lattices and one-dimensional (1D) system, with relatively few studies in 2D square lattices. And the realization of synthetic Weyl points is based on square-lattice valleylike materials, which helps to deepen the research on valleylike materials. Additionally, certain past studies may have drawbacks, such as insufficient bandwidth. So, it is highly desirable to extend the implementation of these research to a broader range of lattice structures.

It is well established that in 2D graphene-lattice PC, degenerate points exist at the K and K' points within the first Brillouin zone.[44–52] However, for 2D square lattices, degeneracy points may not necessarily occur at high-symmetry points due to accidental degeneracies, and the degeneracies are lifted to establish a comprehensive band gap upon the height of not equivalent resonators.[53–58] We treat the rotation angle as an additional dimension and observe synthetic Weyl points in the 3D synthetic space. Within a specific range of angular variation, we observe that the frequency of the topological edge states exhibits a monotonic shift. Apart from the angle, the distance between the sample and the hard boundary also affects the frequency of topological edge states. Over a defined range of distances, the frequency of the topological edge states

†Corresponding author. E-mail: xyzou@nju.edu.cn

© 2025 Chinese Physical Society and IOP Publishing Ltd. All rights, including for text and data mining, AI training, and similar technologies, are reserved.

undergoes a monotonic variation. Based on the above two discoveries, we can design two different types of topological rainbow concentrators. The topological rainbow concentrators we fabricated possess a wide frequency range and the ability to utilize both the upper and lower boundaries for transmission, which exhibits high flexibility.

2. Methods and experiment

2.1. Synthetic Weyl points and the corresponding edge states

As shown in Fig. 1(a), we construct a square-latticed PC by embedding four-legged polymeric scatterers (white regions) in an air medium (blue region). The lattice constant $a = 4.8$ cm, and other parameters of the scatterer are a length l of 3.12 cm and a width b of 1.44 cm. A rotational angle is denoted by the angle θ with respect to y axis, which can control the spatial symmetry and band gap of the system. The rotation of the scatter in a clockwise direction is denoted by $\theta < 0$, whereas a counterclockwise rotation is indicated by $\theta > 0$. The region outlined in red is the unit cell, which can be described by an effective Hamiltonian to characterize the energy of the scattering system. In our work, the simulations are performed by the finite-element commercial software COMSOL MULTIPHYSICS. The mass density and the wave velocity of the air are 1.21 kg/m^3 and 343 m/s, respectively.

We only consider $\theta \in [-45°, 45°]$, where 90° is the period of the scatterers. Figure 1(b) depicts the dispersion relationship of the PC when the rotation angle $\theta = 0°$. In the PC, two Dirac cones emerge at the lines M–Γ and X–M of the Brillouin zone respectively between the fourth and fifth bands. According to the effective Hamiltonian and group theory, the emergence of the Dirac point is attributed to the unavoidable band crossing which is intrinsically protected by the mirror symmetry. When the scatterer rotates clockwise or counterclockwise, the mirror symmetry is broken, thus resulting in the emergence of bandgap. As the rotational angle θ can control the dispersion relation of the square-latticed PC and exhibit periodicity, it can be considered as an additional degree of freedom. A combination of structural parameter θ and Bloch wave vector k_x, k_y forms a 3D linear synthetic space (k_x, k_y, θ). This system possesses both time-reversal symmetry and space-inversion symmetry simultaneously, therefore the Berry curvature can be written as

$$\Omega(\boldsymbol{k}) = \sum_i n_i \pi \delta(\boldsymbol{k} - \boldsymbol{k}_i).$$

Here, $\boldsymbol{k}$ is the momentum of a state, $\delta(\boldsymbol{k} - \boldsymbol{k}_i)$ are the delta functions which are known as Berry fluxes.[56] For this system, the Berry fluxes can take the value of 0 and π. If a Dirac point emerges, the Berry flux is π. When the structural parameters are altered, the Dirac point shifts in the Brillouin zone. Distributions of the Weyl points in the synthetic space (k_x, k_y, θ) are shown in Fig. 1(c). The red solid sphere represents that the topological charge carried by the Weyl point is +1 (more details can be found in Appendix A). The blue markers indicate the positions of the high-symmetry points M and X located within the Brillouin zone. When the structural parameters are at appropriate values, the Dirac points on the Brillouin zone boundary will move to the M point, resulting in the formation of a Weyl point with a topological charge of 2 at the M point in the synthetic space. Figures 1(d) and 1(e) show the 3D band structures in the synthetic space. To be specific, figure 1(d) depicts the relationship between frequency and k_y as well as angle when $k_x = \pi/a$. Figure 1(e) illustrates how frequency varies with angle and k_x when $k_y = 0.275\pi/a$. In this structure, the position of the Weyl point occurs at $(\pi/a, 0.275\pi/a, 0)$ at the frequency of 8004 Hz. The band around the Weyl point is linear along all directions, so the degenerate point is a single Weyl point with topological charge +1.

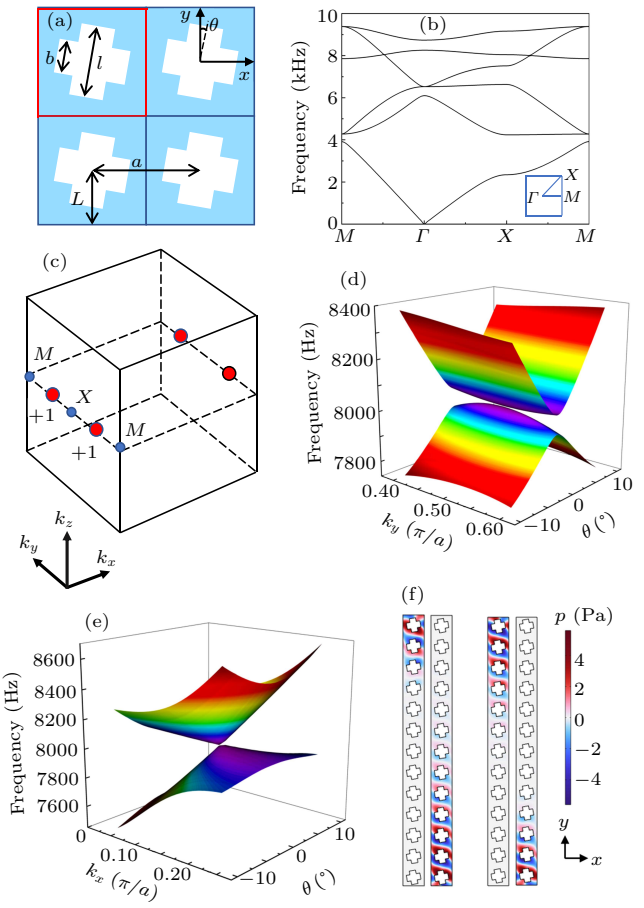


Fig. 1. Weyl points synthesized by 2D square-lattice PC. (a) Schematic diagram of the 2D square-latticed PC. (b) The dispersion relations of the PC with $\theta = 0°$. The inset shows the first Brillouin zone. (c) Distributions of the Weyl points in the synthetic space (k_x, k_y, θ). The red solid sphere represents that the topological charge carried by the Weyl point is +1. (d) Relationship between frequency and k_y as well as θ when $k_x = \pi/a$. (e) Relationship between frequency and k_x as well as θ when $k_y = 0.275\pi/a$. (f) The pressure-field distributions of two edge states in 1×13 supercell of the upper and lower boundaries. Left half: the eigenfrequencies of the upper and lower boundary states are 8317.4 Hz and 8270.3 Hz, respectively, with a rotation angle $\theta = 10°$. Right half: the eigenfrequencies of both the upper and lower boundary states are identical (8299.3 Hz) in the case of $\theta = 10°$.

Previous works[38–41] have revealed the existence of edge states between PC and hard boundaries in this system. Figure 1(f) depicts the supercell we designed, which we utilize to investigate the topological properties of edge states. The supercell includes 13 unit cells with $\theta = 10^\circ$. We consider the position where $y = 0$ as the lower boundary and the position where $y = 13a$ as the upper boundary. As depicted in Fig. 1(a), L is the distance from the center of the first unit cell to the lower boundary. The upper and lower boundaries of the supercell are subjected to hard boundary conditions, while the left and right boundaries are subjected to periodic boundary conditions. The right panel of Fig. 1(f) illustrates the acoustic pressure of the supercell edge state when the scatterer is equidistant from the upper and lower boundaries, that is, the distance from the center of the first unit cell to the lower boundary is the same as the distance from the center of the last unit cell to the upper boundary. As the distance is reduced from 2.16 cm to 1.96 cm, the acoustic pressure of the supercell edge state transforms to that as shown on the left side of Fig. 1(f), with distinct eigenfrequencies for the edge state. As shown in Fig. 1(f), the group velocity of the both lower and upper edge states are positive (right ward) and the projected band structure of the supercell is included in the Appendix B.

2.2. Two methods for constructing topological rainbow concentrators

The frequency of the boundary state within the supercell depends on both the rotation angle and the distance between the scatterer and the hard boundary, which reminds us to design two different rainbow concentrators. As shown in Fig. 2(a), we design a gradient PC structure to study the rainbow trapping. The PC has 16 periods in the x direction and 13 periods in the y direction, where the rotation angle θ decreases from 20° in the first column to 5° in the last column. The rotational interval $\Delta\theta = -1^\circ$ and the distance L from the center of the first primitive cell to the lower boundary of the supercell is 2.16 cm. A point sound source with frequency ranges from 8000 Hz to 8500 Hz, is applied on the left side of the structure (red star in Fig. 2(a)). In addition, the hard boundary condition is applied on the upper and lower boundaries of the PC structure while the left and right boundaries are radiative boundaries.

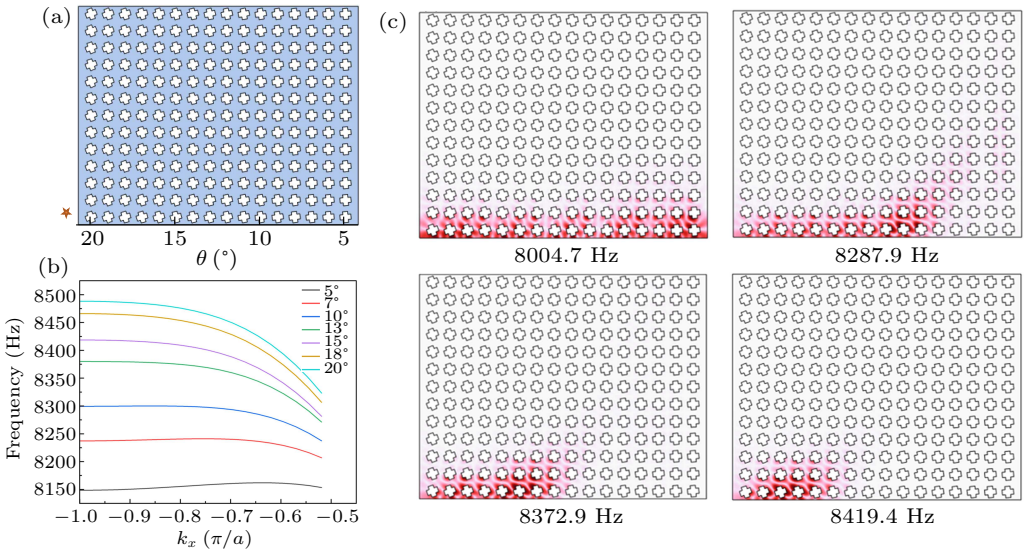


Fig. 2. A topological rainbow concentrator based on rotation gradient. (a) Schematic diagram of the topological rainbow concentrator. The rotation angle θ of the scatterer decreases in a gradient from 20° in the first column to 5° in the last column. The orange stars represent point sound sources. (b) Dispersion relations of the edge states at the lower boundary corresponding to seven different θ. (c) Pressure-field distributions of the edge states corresponding to different frequencies.

We now focus on topological edge states at the lower boundary of the 1×13 supercell. As the rotational angle θchanges, the frequency of the edge state on the lower boundary monotonously varies. For our system, the dispersion relation is symmetric about $k_x = 0$, thus we only need to study the left half or the right half of the dispersion relation. At $k_x = -\pi/a$, with an increase in the angles, the frequencies of the edge states on the lower boundary monotonously increases, as shown in Fig. 2(b). Here, the rotational angles θ are chosen as 5°, 7°, 10°, 13°, 15°, 18°, and 20°, respectively. The characteristic of monotonic variation in the frequency of edge states on the lower boundary plays a crucial role in the design of topological rainbow concentrators. At $k_x = 0$, the frequency of the artificial Weyl point is 8004 Hz, which is less than the frequency of the edge state and close to the frequency of the bulk band. As the angle decreases, the eigenfrequency of the supercell edge state decreases, and eventually approaches the frequency of the Weyl point.

Figure 2(c) shows the sound pressure field distribution around the lower boundaries of the PC at four different frequencies. By observing the sound pressure at these frequencies, we can see the topological rainbow. The first panel in Fig. 2(c) shows the sound pressure at the Weyl point frequency, and it can be observed that the acoustic wave can propagate

from the left boundary to the right boundary. However, as the frequency of acoustic source signal increases, the propagation distance of the acoustic waves decreases. It is noted that when acoustic waves pass through the sample, the acoustic pressure in the vicinity of the point where wave propagation ceases is slightly higher than that at locations further upstream, indicating a mild concentration of energy at this site. As a result, the rotation angle θ can be used to manipulate the edge states propagation of the supercell.

Another method to alter the frequency of edge states is to adjust the distance L from the center of the first unit cell to the lower boundary of the supercell. In Fig. 3(a), the other gradient PC structure is designed to study the rainbow trapping. The size of this structure is identical to the previous one, with 13 rows and 16 columns. We set the rotation angle θ at 10°. The distance L increases from 1.86 cm in the first column to 2.16 cm in the last column, and the interval of the boundaries between the two closest columns $\Delta L = 0.02$ cm. Over this specific distance interval, the group velocities of the lower edge states within the supercell are consistently oriented in a uniform direction, proceeding to the right. We denote the distance in the n-th column as $L_n = 1.86 + \Delta L\,(n-1)$. The boundary conditions and the position of the sound source are the same as the previous structure.

We continue to focus our attention on the frequencies of the edge state at the lower boundary. Six distinct distances L are selected to demonstrate the frequency shift of the edge states. When the distance L increases, the frequency of the edge state on the lower boundary monotonously decreases at $k_x = -\pi/a$ as shown in Fig. 3(b). The frequency range of six edge states monotonously decreases from 8300 Hz to 8190 Hz, so we can design a rainbow collector within this frequency range based on this property.

In Fig. 3(c), four frequencies are selected to show the topological rainbow concentrator and we can see that the edge state at different frequencies stops at different positions. Moreover, as the frequency increases, the position where the sound stops shifts monotonously to the left of the right boundary. Consequently, the distance L can also manipulate the transmission of the supercell edge states. By comparing these two methods, we find that the device obtained from the first method has a broader frequency range, whereas the device from the second method exhibits less concentrated energy (the sound pressure field of the edge states are more widely distributed in the vertical direction). Additionally, we can utilize the upper edge states to design topological rainbow concentrators, with the proviso that the direction of the group velocity must be considered during the design process.

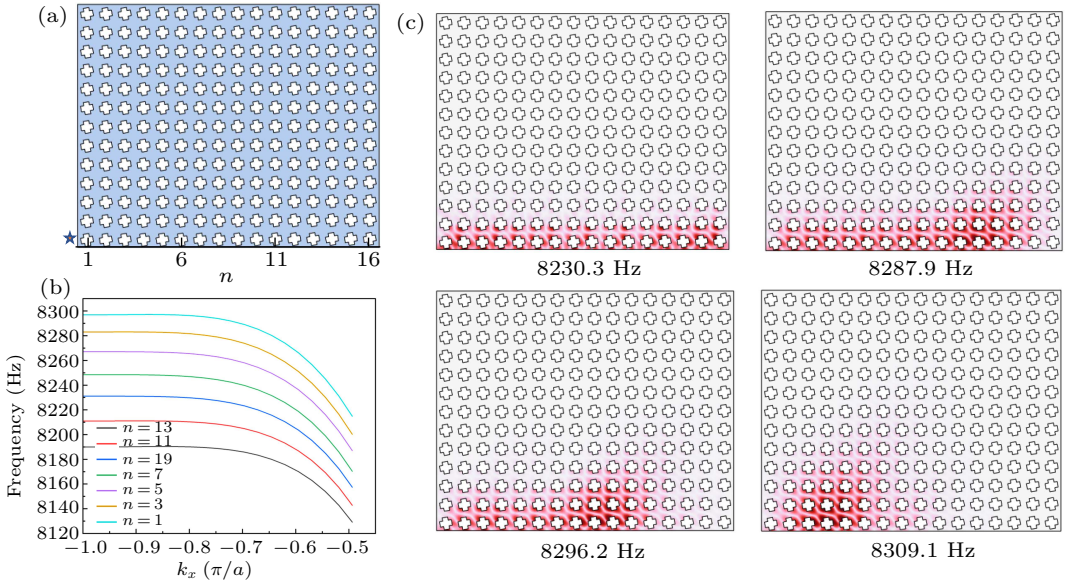


Fig. 3. A topological rainbow concentrator based on different L. (a) Schematic diagram of the topological rainbow concentrator. The value of L in each column decreases by ΔL compared to the previous column. (b) Dispersion relations of the edge states at the lower boundary corresponding to seven different L. (c) Pressure-field distributions of the edge states corresponding to different frequencies.

2.3. Experimental observation of topological rainbow concentrators

In order to experimentally observe the topological rainbow, we conducted experiments using the first method. The experimental setup is illustrated in Fig. 4(a). The four-legged rods in the PC are precisely manufactured using 3D printing and are connected to rigid thin plates. The sample consists of 16×13 periods of unit cells, which the rotational angle θ reduces from 20° to 5°. The rotational interval $\Delta\theta = -1°$ and the distance $L = 2.16$ cm. In order to make the experimental conditions consistent with the simulation conditions, we set the height of the rigid rod to 1.5 cm and covered the top of the sample with a 5-mm thick polymethyl methacrylate (PMMA) plate. To meet the hard boundary condition, the upper and lower ends of the scatterer are connected to cuboids made of the same material, with the height of 1.5 cm and the thick-

ness of 5 mm. We drilled 30 holes in the PMMA plate close to the lower boundary to insert microphones for measuring sound pressure. The sound source is placed at the star position in Fig. 4(a).

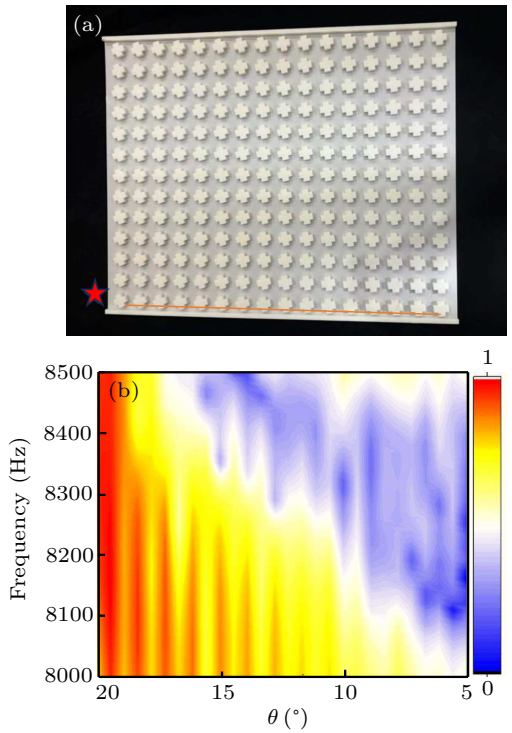


Fig. 4. Experimental observation of topological rainbows formed by angular gradients. (a) Photograph of PC, where the orange line indicates the measurement position. (b) Normalized intensity distributions along the lower boundary.

We have scanned the frequencies from 8000 Hz to 8500 Hz and the responses along the lower boundary (red line) of the sample are obtained as shown in Fig. 4(b), where the abscissa represents the angle decreasing from 20° to 5°, which indicates the transition from the first to the last column of the scatterers. It is observed that as the frequency increases, the propagation distance of the sound wave decreases. The experimental data are in good agreement with the simulation results. Acoustic waves at a frequency of 8419.4 Hz can be effectively trapped at the location corresponding to $\theta = 16°$, which represents the point of the shortest wave propagation distance.

3. Conclusion

In summary, based on the valley-like transport properties in the square lattice, we construct a 3D synthetic space by rotating angles and observe synthetic Weyl points within it. By modulating the rotation and the distance, we propose two types of 2D gradient PC structures to realize topological rainbow concentrators for acoustic waves, and experimentally verify one of them. The results show that acoustic waves of different frequencies will stop at different positions at the lower boundary of the PC. This work presents an alternative approach for precise manipulation of acoustic waves in the frequency and spatial domains.

Appendix A: Calculation of the topological charge of the Weyl points

In this section, we calculate the topological charge of the Weyl points. We use the $k \cdot p$ perturbation to derive the Hamiltonian of the system. Near the crossing point, the effective Hamiltonian is

$$H_{\text{eff}}\left(k_{\parallel}, k_{\perp}\right) = v_0 k_{\parallel}\sigma_0 + v_x k_{\perp}\sigma_x + v_y k_{\perp}\sigma_y + v_z k_{\parallel}\sigma_z,$$

where $k_{\parallel}$ and $k_{\perp}$ represent the vector component parallel and perpendicular to the mirror reflection line, respectively. We use $\Psi = (\psi_{B_2}\, \psi_{A_1}\, \psi_{B_1}\, \psi_{A_2})$ as the basis wave function, which corresponds to the eigenfunction for the third, fourth, fifth, and sixth bands respectively. Then the effective Hamiltonian can be[53]

$$H = \begin{pmatrix} \frac{\omega_{B_2}^2}{c^2} + q_{B_2B_2}\kappa^2 & -p_{B_2A_{1y}}\kappa_y & 0 & -p_{B_2A_{1x}}\kappa_x \\ -p^*_{B_2A_{1y}}\kappa_y & \frac{\omega_{A_1}^2}{c^2} + q_{A_1A_1}\kappa^2 & -p_{A_1B_{2x}}\kappa_x & 0 \\ 0 & -p^*_{A_1B_{2x}}\kappa_x & \frac{\omega_{B_1}^2}{c^2} + q_{B_1B_1}\kappa^2 & -p_{B_1A_{2y}}\kappa_y \\ -p^*_{B_1A_{2x}}\kappa_x & 0 & -p^*_{B_1A_{2y}}\kappa_y & \frac{\omega_{A_2}^2}{c^2} + q_{A_2A_2}\kappa^2 \end{pmatrix},$$

where $\boldsymbol{\kappa} = k - k_0$, c is the speed of sound, ω_i is the eigen frequency at M. The coefficient is

$$p_{ljx} = \mathrm{i}\frac{(2\pi)^2}{\Omega}\int \psi^*_{lk_0}(\boldsymbol{r}) \cdot 2\frac{\partial}{\partial x}\psi_{jk_0}(\boldsymbol{r})\,\mathrm{d}\boldsymbol{r}, \quad p_{ljy} = \mathrm{i}\frac{(2\pi)^2}{\Omega}\int \psi^*_{lk_0}(\boldsymbol{r}) \cdot 2\frac{\partial}{\partial y}\psi_{jk_0}(\boldsymbol{r})\,\mathrm{d}\boldsymbol{r}, \quad q_{lj} = \mathrm{i}\frac{(2\pi)^2}{\Omega}\int \psi^*_{lk_0}(\boldsymbol{r}) \cdot \psi_{jk_0}(\boldsymbol{r})\,\mathrm{d}\boldsymbol{r}.$$

Here Ω is the area of the unit cell. Basis wave function can be extracted from COMSOL Multiphysics, and the data processing is conducted using COMSOL with MATLAB. Then, we integrate the Berry curvature over an enclosing surface, this enclosing surface is a cube that encapsulates the Weyl point. $C = \frac{1}{2\pi}\int F(k) \cdot \mathrm{d}S$, where $F(k) = \mathrm{i}\langle\nabla_{\boldsymbol{k}} u(\boldsymbol{k})| \times |\nabla_{\boldsymbol{k}} u(\boldsymbol{k})\rangle$. In our case, $u(k) = \psi_{B_1}$. Our calculations show that $C = 1$ of the fifth band.

Appendix B: Projected band of the supercell

In this section, we show in Fig. B1 the projected band of the supercell in Fig. 1(f). It can be seen that when the scatterer is equidistant from the upper and lower boundaries, the group velocities of the upper and lower edge state have the same direction and magnitude. When the distance changes, the group velocities of the edge state maintain the same direction but differ in magnitude.

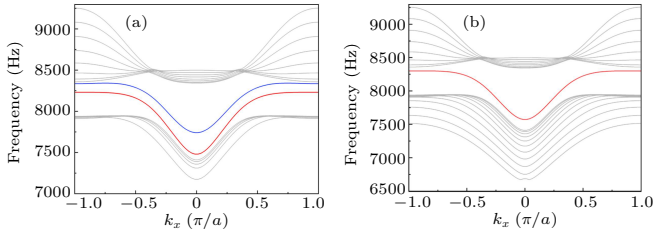


Fig. B1. Projected band of the supercell. (a) Projected band of the supercell shown in the left panel of Fig. 1(f). (b) Projected band of the supercell shown in the right panel of Fig. 1(f).

Acknowledgements

Project supported by the National Natural Science Foundation of China (Grant Nos. 12074184, 12274219, and 11934009) and the Key Research and Development Project of Jiangsu Province, China (Grant No. BE2022814).

References

[1] Tsakmakidis K L, Boardman A D and Hess O 2007 *Nature* **450** 397
[2] Lu C, Wang C, Xiao M, Zhang Z Q and Chan C T 2021 *Phys. Rev. Lett.* **126** 113902
[3] Zhang H, Qian L, Wang C, Ji C Y, Liu Y, Chen J and Lu C 2021 *Opt. Lett.* **46** 1237
[4] Lu C, Sun Y Z, Wang C, Zhang H, Zhao W, Hu X, M. Xiao, Ding W, Liu Y C and Chan C T 2022 *Nat. Commun.* **13** 2586
[5] Xu Q, Peng Y, Shi A, Peng P and Liu J 2024 *J. Opt. Soc. Am. A* **41** 366
[6] Zhao J, Wu X, Zhang D, Xu X, Wang X and Zhao X 2024 *Nat. Commun.* **15** 2613
[7] Wu H, Yin Y, Sheng Z, Li Y, Qi D and Peng R 2021 *Phys. Rev. Appl.* **15** 054033
[8] Wang Z, Wang Z, Li H, Liu Z, Luo J, Huang F, Wang X, Li H and Yang H 2022 *Phys. Rev. Appl.* **17** 064002
[9] Guan A Y, Yang Z Z, Yang W J, Li S F, Zou X Y and Cheng J C 2022 *Phys. Rev. Appl.* **18** 044054
[10] Liu C, Zhang Z, Liao D, Yue Z, Ma C, Cheng Y and Liu X 2023 *Appl. Phys. Lett.* **123** 041701
[11] Tang X L, Ma T X and Wang Y S 2023 *Appl. Phys. Lett.* **122** 112201
[12] Ponti J M D, Colombi A, Adrito R, Braghin F, Corigliano A and Craster R V 2020 *New J. Phys.* **22** 013013
[13] Chaplain G J, De Ponti J M, Aguzzi G, Colombi A and Craster R V 2020 *Phys. Rev. Appl.* **14** 054035
[14] Ungureanu B, Makwana M P, Craster R V and Guenneau S 2021 *Phys. Rev. Appl.* **15** 014057
[15] Gu Y, Jiang K, Wu X and Hu J 2022 *Chin. Phys. Lett.* **39** 097401
[16] Yu Q H and Lin Z J 2024 *Chin. Phys. Lett.* **41** 030202
[17] Li Han, Wang Z, Fan S, Li H, Yang H and Wen H 2024 *Chin. Phys. Lett.* **41** 057402
[18] Yi J and Chen C Q 2024 *New J. Phys.* **26** 063004
[19] Ding W, Zhang R, Chen T, Qu S, Yu D, Dong L, Zhu J, Yang Y and Assouar B 2024 *Commun. Phys.* **7** 272
[20] Soltani A, Mousavi S. F, Firouzeh1 Z H, Nezhad A Z and Nouroozi R 2024 *Sci. Rep.* **14** 21272
[21] Zhong H, Kompanets V O, Zhang Y, Kartashov Y V, Cao Meng, Li Y, Zhuravitskii S A, Skryabin N N, Dyakonov I V, Kalinkin A A, Kulik S P, Chekalin S V and Zadkov V N 2024 *Light Sci. Appl.* **13** 264
[22] Shi A, Peng Y, Peng P, Chen J and Liu J 2024 *Phys. Rev. B* **110** 014106
[23] Wu X, Chen Z, Bai Y, Huang B, Dai Y and Niu C 2024 *Phys. Rev. B* **109** 235407
[24] Liu D, Peng P, Lu X, Shi A, Peng Y, Wei Y and Liu J 2024 *Opt. Lett.* **49** 2393
[25] Shi A Q, Peng Y W, Jiang J P, Peng Y C, Peng P, Chen J Z, Chen H S, Wen S C, Lin X, Gao F and Liu J J 2024 *Laser Photon. Rev.* **18** 2300956
[26] Chen J, Shi A, Peng Y, Peng P and Liu J 2024 *Chin. Phys. Lett.* **41** 037103
[27] Xu W, Zhang X, Liu M, Li Y, Wang Y and Wang Q 2024 *Appl. Phys. Lett.* **124** 051702
[28] Xiao M, Chen W, He W and Chan C 2015 *Nat. Phys.* **11** 920
[29] Chen W, Xiao M and Chan C 2016 *Nat. Commun.* **7** 13038
[30] Ge H, Ni X, Tian Y, Gupta S K, Lu M H, Lin X, Huang W D, Chan C T and Chen Y F 2018 *Phys. Rev. Appl.* **10** 014017
[31] He H, Qiu C, Ye L, Cai X, Fan X, Ke M, Zhang F and Liu Z 2018 *Nature* **560** 61
[32] Li F, Huang X, Lu J, Ma J and Liu Z 2018 *Nat. Phys.* **14** 30
[33] Chen T G, Jiao J R, Dai H Q and Yu D J 2018 *Phys. Rev. B.* **98** 214110
[34] He H, Qiu C, Cai X, Xiao M, Ke M, Zhang F and Liu Z 2020 *Nat. Commun.* **11** 1820
[35] Huang X, Deng W, Li F, Lu J and Liu Z 2020 *Phys. Rev. Lett.* **124** 206802
[36] Wang Q, Xiao M, Liu H, Zhu S and Chan C 2017 *Phys. Rev. X* **7** 031032
[37] Fan X, Qiu C, Shen Y, He H, Xiao M, Ke M and Liu Z 2019 *Phys. Rev. Lett.* **122** 136802
[38] Wang Z, Wang Z, Li H, Luo J, Wang X, Liu Z and Yang H 2021 *Appl. Phys. Express* **14** 077002
[39] Xu C, Zheng T, Ge H, Wang W, Chen Z G, Lu M H and Chen Y F 2022 *Sci. Bull.* **67** 1950
[40] Fan X, Xia T, Qiu H, Zhang Q and Qiu C 2022 *Phys. Rev. Lett.* **128** 216403
[41] Zhang X, Deng C, Yang Y, Li J, Yu Y and Yang H 2024 *Appl. Phys. Lett.* **124** 163101
[42] Zheng L, Qin C, Zhu X F, Chen S, Zhao L, Liu Z, Liu W, Wang B and Lu P 2024 *Phys. Rev. Appl.* **21** 054048
[43] Ye L, Wang Q, Fu Z, He H, Huang X, Ke M, Lu J, Deng W and Liu Z 2024 *Phys. Rev. Lett.* **133** 126602
[44] Lu J, Qiu C, Ke M and Liu Z 2016 *Phys. Rev. Lett.* **116** 093901
[45] Lu J, Qiu C, Ye L, Fan X, Ke M, Zhang F and Liu Z 2017 *Nat. Phys.* **13** 369
[46] Zhang Z, Wei Q, Cheng Y, Zhang T, Wu D and Liu X 2017 *Phys. Rev. Lett.* **118** 084303
[47] Lu J, Qiu C, Deng W, Huang X, Li F, Zhang F, Chen S and Liu Z 2018 *Phys. Rev. Lett.* **120** 116802
[48] Wang M, Ye L, Christensen J and Liu Z 2018 *Phys. Rev. Lett.* **120** 246601
[49] Zhang Z W, Tian Y, Wang Y H, Gao S X, Cheng Y, Liu X J and Christensen J 2018 *Adv. Mater.* **30** 1803229
[50] Shen Y, Qiu C, Cai X, Ye L, Lu J, Ke M and Liu Z 2019 *Appl. Phys. Lett.* **114** 023501
[51] Yan B, Peng Y W, Xie J L, Peng Y C, Shi A Q, Li H, Gao F, Peng P, Jiang J P, Liu J J, Gao F and Wen S C 2024 *Laser Photon. Rev.* **18** 2300686
[52] Li S F, Lu J Y, Zhou C Y Y, Zou X Y and Cheng J C 2024 *Phys. Rev. Appl.* **22** 034025
[53] He W Y and Chan C T 2015 *Sci. Rep.* **5** 8186
[54] Xu C, Fang A, Chu H, Luo J, Chan C T, Hang Z H and Lai Y 2016 *Phys. Rev. B* **93** 245116
[55] Miert G van and Smith C M 2016 *Phys. Rev. B* **93** 035401
[56] Xia B Z, Zheng S J, Liu T T, Jiao J R, Chen N, Dai H Q, Yu D J and Liu J 2018 *Phys. Rev. B* **97** 155124
[57] Zhu Z, Huang X, Lu J, Yan M, Li F, Deng W and Liu Z 2019 *Phys. Rev. Appl.* **12** 024007
[58] Zhu Z, Yan M, Pan J, Yang Y, Deng W, Lu J, Huang X and Liu Z 2021 *Phys. Rev. Appl.* **16** 014058